Supplementary Information for:
Time dependence of advection-diffusion coupling for nanoparticle ensembles

Alexandre Vilquin, Vincent Bertin, Pierre Soulard, Gabriel Guyard,
Elie Raphaël, Frédéric Restagno, Thomas Salez and Joshua D. McGraw

Supplementary document information

- Video 1: Image sequences of raw experimental data for 55 nm-radius fluorescent particles advected in a pressure driven flow of pure water along a microchannel with geometry described in the text, and with an incident 488 nm-laser angle of 64 °. The videos were taken with pressure drops imposed as noted, and each frame has a width of 23 μm.

- Video 2: Identical to Video 1 but with particle trajectories superimposed.

- Video 3: Animations of particle trajectories obtained from Langevin simulations imposing 'dot', 'half-line' and 'line' initial conditions (indicated by the black regions, see main text for definitions), with diffusion along the vertical and shear flow advection along the horizontal. The animation is displayed during a dimensionless time range $0 \leq \tau/\tau_z \leq 0.1$ in the lab frame.

- Video 4: [Left] Identical to Video 3, but in the reference frame of the center of mass for the fluid and for a dimensionless time range $0 \leq \tau/\tau_z \leq 10$. The horizontal black-outlined bar in the middle panel indicates the entire observation zone at $\tau/\tau_z = 10$, and the observed region at a given instant is highlighted in red. [Right] For the three different conditions of the right panels, progression of the reduced dispersion coefficient.

- *TaylorDispersion.html*: Python/Jupyter notebook describing the overdamped Langevin simulations of Section 7, in particular reproducing Figs. S3 and S4.

1 Notations used in the main text

Coordinates

x	streamwise coordinate, direction of flow
y	transverse coordinate, flow-invariant
z	wall-normal coordinate

Times

t	particle observation time
τ	lag time
τ_z	channel exploration time
τ_{C}	early-time 'line-dot' crossover time

Diffusion coefficients and dispersions

D_0	bulk isotropic diffusion coefficient
D_y	diffusion coefficient in flow-invariant direction
$\mathcal{D}_x$	dispersion coefficient in the flow direction
$\mathcal{D}_{\langle n \rangle}$	dispersion coefficient in the flow direction averaged over a fraction, n of H
$\mathcal{D}_{\tau_{\max}}$	$\mathcal{D}_{\langle 1/2 \rangle}$ at late experimental times
$\mathcal{F}_{\langle n \rangle}$	reduced dimensionless analogue of $\mathcal{D}_{\langle n \rangle}$

Statistical quantities

$\mathcal{P}$	probability distribution functions
$\langle z_0 \rangle$	first moment of $\mathcal{P}_0(z_0)$
$\langle z_0^2 \rangle$	second moment of $\mathcal{P}_0(z_0)$
$\sigma_{[]}$	standard deviation of quantity $[]$

Experimental parameters

a	particle radius
η	fluid viscosity
ρ	fluid density
h	channel height
w	channel width
ℓ	channel length
H	observation domain size
n	fraction of observed flow domain
ΔP	pressure drop across channel length
v_x	flow speed along the x-direction
$\dot{\gamma}$	near-wall shear rate
U	average flow speed in Poiseuille flow
Re	Reynolds number
Pe	Péclet number
α	Taylor's geometric dispersion factor
λ	illumination laser wavelength
n_{f}	index of refraction: fluid
n_{g}	index of refraction: glass substrate
θ	incident laser angle
θ_{c}	critical incident angle
Π	evanescent wave penetration length
I	particle fluorescence intensity
I_0	particle fluorescence intensity at the solid/liquid interface

2 Intensity distribution and mean velocity profiles

This section provides additional information about how the observed signal intensity distributions (SIDs after Zheng and coworkers [1], denoted $\mathcal{P}_{\text{SID}}$) and the corresponding velocity profiles can be quantitatively described simultaneously. As also described by Li and coworkers [2], fluorescent nanoparticles detected have a limited range of intensities affected by several factors, the most important ones being, and as discussed in turn: *i*) electrostatic interactions which determine the probability that a particle of a given radius is found at a certain distance from the wall according to a Boltzmann distribution; *ii*) particle size distribution; and *iii*) the optical setup which, given the position and size of the particle, finally determines its intensity. We now discuss each of these elements in detail.

–*i*– The glass surface exerts an electrostatic repulsion on the particles according to the fact that both surfaces are negatively charged; the details of such a repulsion are understood within the Derjaguin-Landau-Verwey-Overbeek (DLVO) framework [3, 4]. This electrostatic interaction potential, ϕ_{el}, describing the electric double-layer repulsion between a particle with radius R and a flat wall [5] is given by:

$$\phi_{\text{el}}\left(z_{\text{c}}\right) = 16\epsilon R \left(\frac{k_{\text{B}}T}{e}\right)^2 \tanh\left(\frac{e\psi_{\text{p}}}{4k_{\text{B}}T}\right) \tanh\left(\frac{e\psi_{\text{w}}}{4k_{\text{B}}T}\right) \exp\left(-\frac{z_{\text{c}} - R}{l_{\text{D}}}\right). \qquad \text{(S1)}$$

Here, z_{c}, ϵ, e, ψ_{p}, ψ_{w} and l_{D} are respectively the position of the center of the particle, liquid permittivity, elementary charge, particle and wall electrostatic potentials and the Debye length. This interaction determines the particle concentration C at thermal equilibrium through the Boltzmann distribution

$$C(z_{\text{c}}) \propto \exp\left(-\frac{\phi_{\text{el}}\left(z_{\text{c}}\right)}{k_{\text{B}}T}\right) . \qquad \text{(S2)}$$

As already observed in TIRFM experiments, the van der Waals interaction can be neglected for pure water [1, 2]. Consequently, the typical distance between the bottom surface (located at $z = 0$) and the particles is mainly determined by the Debye length.

–*ii*– All the particles do not have the same radius R. The radius distribution is usually described by a Gaussian probability function

$$\mathcal{P}_R\left(R\right) = \frac{1}{\sqrt{2\pi\sigma_R^2}} \exp\left(-\frac{(R-a)^2}{2\sigma_R^2}\right) , \qquad \text{(S3)}$$

where a is the mean radius and σ_R its standard deviation.

–*iii*– The fluorescence intensity, I, of an individual particle is determined by the optical parameters of the TIRFM setup and the particle's size, with $I \propto R^3$. The evanescent wave has a penetration depth Π characterizing the exponential decrease of excitation. The observed fluorescence intensity is also sensitive to the finite depth of field, d_{f}, of the microscope objective. In our experiments, the depth of field has a value of 415 nm, meaning that if particles are not located on the focal plane at z_{f} (typically 400-500 nm from the glass-liquid interface), they will be detected with a relatively low intensity. Putting these elements together, the observed fluorescence intensity for an individual particle is predicted [1] as

$$\frac{I\left(R, z_{\text{c}}\right)}{I_0} = \left(\frac{R}{a}\right)^3 \exp\left(-\frac{z_{\text{c}} - R}{\Pi}\right) \left[1 + \left(\frac{z_{\text{c}} - R - z_{\text{f}}}{d_{\text{f}}}\right)^2\right]^{-1} , \qquad \text{(S4)}$$

where I_0 is the intensity for a particle with radius $R = a$ located at the bottom surface $z_{\text{c}} = a$ and with the focal plane at the wall ($z_{\text{f}} = 0$).

Using a home-made MATLAB interface, we combine Eqs. S1-S4 to generate theoretical SIDs numerically. Practically, we determine the fraction of particles having an altitude z_{c}
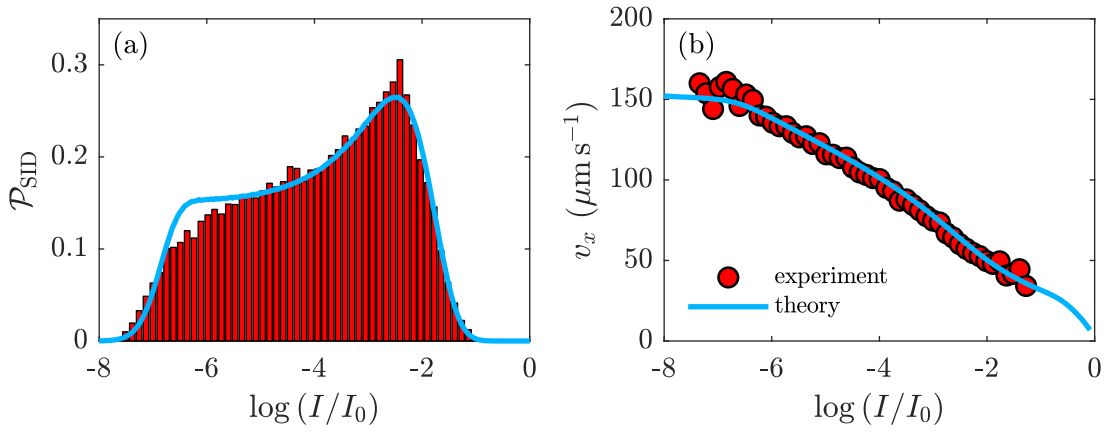
Figure S1: *(a) Comparison between experimental and theoretical signal intensity distributions (SIDs). (b) Comparison between experimental and theoretical streamwise mean velocity profiles. The experimental data is for 55 nm-radius particles for a pressure drop of 30 mbar across the microchannel.*

and a radius R given by the weight $W(z_c, R) = C(z_c)\mathcal{P}_R(R)$, and compute the associated intensity given by Eq. S4. This procedure gives a list of weighted intensities forming the blue line shown in Fig. S1(a) using a DLVO prefactor $16a\epsilon(k_BT/e)^2 \tanh(e\Psi_p/4k_BT)$ $\tanh(e\Psi_w/4k_BT) = 1.4 \times 10^{-21}$ J, $l_D = 60$ nm, $\sigma_R = 5.5$ nm, $a = 55$ nm and the optical parameters as described above, along with the experimental histogram (red).

In addition, we also quantitatively describe the mean streamwise velocity profile, which, as noted before [2], is not perfectly linear when using the apparent altitude $z = z_c - a = \Pi \ln(I_0/I)$ defined in the main article. We assume that a particle located at an altitude z_c has a mean streamwise velocity v_x given by $v_x(z) = f_B\dot{\gamma}z$, where $\dot{\gamma}$ is the shear rate and f_B the "Brenner factor" [6]. This factor provides the hydrodynamic correction induced by the finite size of the spherical particle, when the latter is advected by a linear shear flow near a wall. For large z_c/R, the Brenner factor can be expressed as $f_B \simeq 1 - (5/16)(z_c/R)^{-3}$. For 55 nm-radius particles typically located at distances larger than 200 nm due to electrostatic repulsion, the deviation from the linear velocity profile is less than 1%.

Using the proposed particle velocity profile in conjunction with the intensity-altitude-probability relations (Eqs. S1-S4), we follow Zheng *et al.* [1] and predict the particle's mean streamwise velocity as a function of $\log(I_0/I)$. Such a prediction is made with $\dot{\gamma}$ adjusted simultaneously to the physical and optical parameters of Eqs. S1-S4. The result is shown together with the experimental results in Fig. S1(b), showing good agreement and capturing the main nonlinear features of the experimental data. The shear-rate values obtained with this SID method are approximately 15% smaller than the ones directly obtained using a linear regression of the velocity profiles of Fig. 1(c) using the apparent altitude. This discrepancy is mainly due to the particle polydispersity and to the finite depth of field of the microscope objective, and since it is only a constant factor (verified) across all experiments it does not change the main conclusions of the article.

3   Medium viscosity and particle diffusion

In Fig. 1(c), we show the streamwise velocity profiles for 55 nm-radius particles in a water flow obtained by total internal reflection fluorescence microscopy (TIRFM). In the corresponding inset, we show the associated shear rate $\dot{\gamma}$ (obtained from a linear regression on a given velocity profile) as a function of the pressure drop ΔP across the channel. Similar measurements were done for the 100 nm-radius particles in water and water-glycerol mixtures presented in the main article, see Figs. 3 and 4. Corresponding to these shear rate measurements, we can compute the stress, $\Sigma = h\Delta P/2\ell$, from the pressure
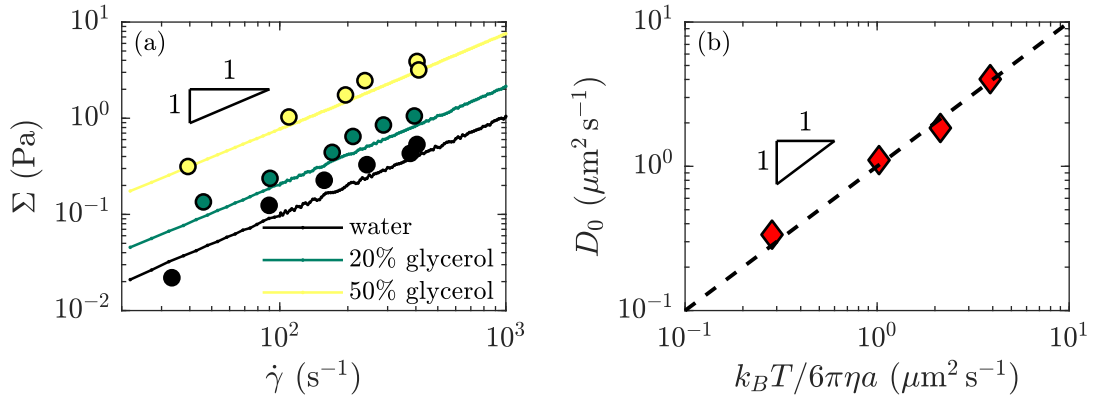
Figure S2: *(a) Comparison for stresses Σ versus shear rate $\dot{\gamma}$ between TIRFM (circles) and rheology measurements (lines) for 100 nm-radius particles, see inset of Fig. 1(c) for $a = 55$ nm particles in water. For TIRFM, the stress is calculated as $\Sigma = h\Delta P/2\ell$ where ΔP is the pressure gap in the channel, h and ℓ are the channel height and length. (b) Bulk diffusion coefficient D_0, measured from the plateau values of local transverse mean square displacements, versus the theoretical values calculated using the viscosity measured with a rheometer, for all particle sizes and water-glycerol mixtures. The black dashed line shows the linear relation with unit prefactor.*

drop across the rectangular channel using a geometric prefactor (height $h = 18$ μm, width $w = 180$ μm, length $\ell = 8.8$ cm). The stress Σ is plotted as a function of the shear rate $\dot{\gamma}$ in Fig. S2(a) and compared with bulk rheology measurements carried out in a Couette cell (see Methods). First, the resulting linear power laws show that all the solutions remain Newtonian for shear rates up to 1000 s^{-1}. Second, the viscosity defined as $\eta = \Sigma/\dot{\gamma}$ is consequently constant for a given solution, and it increases with the glycerol proportion. The results show a good agreement with the rheology measurements, validating both the shear rate and viscosity values obtained by TIRFM.

The viscosity values obtained further allow us to verify that the bulk diffusion coefficients measured with TIRFM are consistent with the Stokes-Einstein relation. As shown in Fig. 3(a) in the main article, the bulk diffusion coefficient D_0 is obtained from the plateau value of the local transverse diffusion coefficient D_y, calculated from the transverse mean-square displacement $\sigma^2_{\Delta y}$, through: $D_y = \sigma^2_{\Delta y}/2\tau$, where τ is the lag time. In Fig. S2(b) is shown a comparison between the experimental results and the prediction given by the Stokes-Einstein relation [7]: $D_0 = k_{\mathrm{B}}T/6\pi\eta a$, after having used the independent, rheologically measured viscosity. The good agreement validates the statistical method to obtain the bulk diffusion coefficient.

4 Taylor dispersion for a linear shear flow in a channel with a rectangular section: long times

Here, we justify the expression (see Eq. 1 of the main article) of the dispersion coefficient for a linear shear flow in the long-time limit:

$$\mathcal{D}_x = D_0 \left(1 + \frac{1}{120}\frac{\dot{\gamma}^2 H^4}{D_0^2}\right), \quad \tau \gg \tau_z . \tag{S5}$$

The classical Taylor dispersion coefficient is typically calculated for a channel with either a circular or a rectangular section and for a Poiseuille flow [8]. To interpret the results described in Figs. 3 and 4 in the main article, we revisit its derivation for a linear shear flow. First, we consider a population of identical spherical colloids, in a rectangular channel of height H, subjected to a linear shear flow $v_x(z) = \dot{\gamma}z$ along the x-axis, where $\dot{\gamma}$ is a constant

5

shear rate and where $0 \leqslant z \leqslant H$. Thus, the mean velocity along x is $\frac{1}{H} \int_0^H v_x(z)\,\mathrm{d}z = \dot\gamma H/2$. We assume invariance in the y-direction which is valid in the experiments. We also neglect hydrodynamic interactions with the walls, which would introduce a z-dependence of the diffusion coefficients in both the streamwise and wall-normal directions. Therefore, all the colloids are assumed to have the same, bulk diffusion coefficient D_0. The colloidal concentration field $c(x,z,t)$ evolves with time t, from both advection by the imposed flow and diffusion, as described by the advection-diffusion equation:

$$\partial_t c + v_x \partial_x c = D_0\left(\partial_x^2 c + \partial_z^2 c\right). \tag{S6}$$

Introducing the streamwise length scale L, a concentration scale c_0, the dimensionless variables $Z = z/H$, $X = x/L$, $T = tD_0/H^2$, $C(X,Z,T) = c(x,z,t)/c_0$, $V(Z) = v_x(z)/\dot\gamma H$, the Péclet number $\mathrm{Pe} = \dot\gamma H^2/D_0$ and the aspect ratio $\varepsilon = H/L$, Eq. (S6) becomes:

$$\partial_T C + \varepsilon\mathrm{Pe}V(Z)\partial_X C = \varepsilon^2\partial_X^2 C + \partial_Z^2 C. \tag{S7}$$

We decompose the concentration profile through:

$$C(X,Z,T) = \bar C(X,T) + C'(X,Z,T), \tag{S8}$$

with $\bar C(X,T) = \int_0^1 C(X,Z,T)\,\mathrm{d}Z$ the thickness-averaged concentration and C' the deviation from the latter. Inserting this decomposition into Eq. (S7), one obtains:

$$\partial_T \bar C + \partial_T C' + \varepsilon\mathrm{Pe}V(Z)\partial_X \bar C + \varepsilon\mathrm{Pe}V(Z)\partial_X C' = \varepsilon^2\partial_X^2 \bar C + \varepsilon^2\partial_X^2 C' + \partial_Z^2 C'. \tag{S9}$$

Averaging further over Z leads to:

$$\partial_T \bar C + \varepsilon\mathrm{Pe}\frac{1}{2}\partial_X \bar C + \varepsilon\mathrm{Pe}\overline{V\partial_X C'} = \varepsilon^2\partial_X^2 \bar C + \varepsilon^2\overline{\partial_X^2 C'}, \tag{S10}$$

where we assumed no normal colloidal flux at the channel boundary. Subtracting the two last equations with one another gives:

$$\partial_T C' + \varepsilon\mathrm{Pe}\left(V - \frac{1}{2}\right)\partial_X \bar C + \varepsilon\mathrm{Pe}\left(V\partial_X C' - \overline{V\partial_X C'}\right) = \varepsilon^2\left(\partial_X^2 C' - \overline{\partial_X^2 C'}\right) + \partial_Z^2 C'. \tag{S11}$$

Invoking now the long-time condition proposed by Taylor [8], $T \gg 1$, the concentration field becomes nearly homogeneous along Z leading to $C' \ll \bar C$. In addition, we have $\varepsilon \ll 1$. All together, Eq. (S11) can be simplified into:

$$\partial_Z^2 C' \simeq \varepsilon\mathrm{Pe}\left(V - \frac{1}{2}\right)\partial_X \bar C. \tag{S12}$$

Since the thickness-averaged concentration field $\bar C$ does not depend on Z, a first integration gives:

$$\partial_Z C' = \varepsilon\mathrm{Pe}\partial_X \bar C\left(\frac{Z^2}{2} - \frac{Z}{2}\right) + c_1, \tag{S13}$$

where c_1 is a constant. Due to the impermeability of the channel walls, the no-flux boundary conditions are $\partial_Z C'\,|_{Z=0} = 0$ and $\partial_Z C'\,|_{Z=1} = 0$ giving $c_1 = 0$. Thus, the second integration gives:

$$C' = \varepsilon\mathrm{Pe}\partial_X \bar C\left(\frac{Z^3}{6} - \frac{Z^2}{4} + c_2\right). \tag{S14}$$

By definition, the thickness average of the deviation field C' is zero, leading to:

$$C' = \varepsilon\mathrm{Pe}\partial_X \bar C\left[\frac{Z^3}{6} - \frac{Z^2}{4} + \frac{1}{24}\right]. \tag{S15}$$

Invoking the found relation between C' and $\bar{C}$, Eq. (S10) becomes:

$$\partial_T \bar{C} + \frac{1}{2}\varepsilon \mathrm{Pe}\partial_X \bar{C} = \varepsilon^2 \left(1 + B\mathrm{Pe}^2\right) \partial_X^2 \bar{C}, \tag{S16}$$

with B a dimensionless factor given by:

$$B = -\int\limits_0^1 \mathrm{d}Z\, Z \left(\frac{Z^3}{6} - \frac{Z^2}{4} + \frac{1}{24}\right) = \frac{1}{120}. \tag{S17}$$

Putting back the dimensions and adding the definition $\bar{c} = c_0 \bar{C}$, we obtain the final equation for the long-time limit:

$$\partial_t \bar{c} + \frac{\dot{\gamma}H}{2}\partial_x \bar{c} = \mathcal{D}_x \partial_x^2 \bar{c}, \tag{S18}$$

with the dispersion coefficient $\mathcal{D}_x = D_0 \left(1 + B\mathrm{Pe}^2\right)$ where $B = 1/120$. Therefore, at long times, the thickness-averaged colloidal concentration field is advected with the mean velocity $\dot{\gamma}H/2$ and diffuses with the effective diffusion coefficient:

$$\mathcal{D}_x = D_0 \left(1 + \frac{1}{120}\frac{\dot{\gamma}^2 H^4}{D_0^2}\right), \quad \tau \gg \tau_z. \tag{S19}$$

5 Taylor time in a channel with a rectangular section

Here, we justify that the relaxation of an initial concentration profile in a rectangular channel takes place over the time scale τ_z/π^2 where the Taylor time is $\tau_z = H^2/D_0$. This quantity corresponds to the time beyond which the dispersion coefficient, Eq. (S19), calculated above becomes valid. According to Taylor [8], this time scale corresponds additionally to the duration needed to have a homogenous concentration field along z. This phenomenon is only due to the diffusion along z, leading us to solve:

$$\partial_t c = D_0 \partial_z^2 c, \tag{S20}$$

where $c(z,t)$ is the concentration field, the other spatial dependencies being irrelevant. We assume an initial concentration field $c(z, t = 0) = c_0(z)$ and solve the diffusion equation on a domain $z \in [0, H]$ along with impermeability boundary conditions: $\partial_z c(z,t) = 0$ at $z = 0$ and $z = H$. This problem can be solved exactly using the spectral decomposition:

$$c(z,t) = \bar{c} + \sum_{k=1}^\infty a_k(t) \cos\left(\frac{k\pi z}{H}\right), \tag{S21}$$

where $\bar{c}$ denotes the thickness-averaged concentration, and the coefficients a_k follow the linear ordinary differential equations: $\partial_t a_k = -D_0(k\pi/H)^2 a_k$. The general solution of this diffusion problem is

$$c(z,t) = \bar{c} + \sum_{k=1}^\infty a_{k,0} \cos\left(\frac{k\pi z}{H}\right) \exp\left(-\frac{k^2\pi^2 D_0 t}{H^2}\right), \tag{S22}$$

where $a_{k,0} = a_k(0) = (2/H)\int_0^H c_0(z)\cos(k\pi z/H)\,\mathrm{d}z$. As a result, the slowest decaying mode $k = 1$ has a typical decay time $H^2/\pi^2 D_0 = \tau_z/\pi^2$ as desired.

6 Taylor dispersion in a linear shear flow at short times for different initial particle distributions: short times

In this section, we first provide the derivation of the short-term dispersion coefficient for a general distribution of initial particle altitudes in free space, before addressing the particular case of uniform distributions. A central assumption of the model presented in the main article is that the short-time Taylor dispersion in a channel, behaves in the same way as for an infinitely-extended medium. It is supported by the fact that the wall-normal diffusion of a particle in the channel is not affected by the presence of the walls at short times. Therefore, this assumption is valid only for time scales much shorter than the typical time $\tau_z = H^2/D_0$ for diffusion over the channel height, as introduced in the previous section.

6.1 General distribution of initial particle altitudes in free space

In this subsection, we justify how the short-time dispersion coefficient for a unique particle in a linear shear flow [9, 10, 11, 12, 13] $\mathcal{D}_x = D_0 \left(1 + \dot{\gamma}^2 \tau^2/3\right)$, is modified by considering a group of particles leaving from different altitudes z. The single-particle expression, analogous to the 'dot' condition in the main article, is neither valid in our experiments nor in the general case. Thus, we consider particles that are advected in a shear flow after having started at $x = 0$, from different initial altitudes z_0 described by the probability density function (PDF) $\mathcal{P}_0 \left(z_0\right)$. The particles are assumed to diffuse in an infinite space along z. We stress that the hydrodynamic and electrostatic interactions with the wall, which are present in the experiments, are neglected here. We will discuss their effects on the Taylor dispersion in the next section, using Langevin simulations.

The calculation of the dispersion coefficient $\mathcal{D}_x = \sigma^2_{\Delta x}/2\tau$ requires the variance $\sigma^2_{\Delta x} = \left\langle \Delta x^2 \right\rangle - \left\langle \Delta x \right\rangle^2$ of the streamwise displacement $\Delta x \left(\tau\right) = x \left(t + \tau\right) - x \left(t\right)$. We assume here a linear shear flow, with a velocity $v_x \left(z\right) = \dot{\gamma} z$ along x. We do not consider the streamwise Brownian motion since it is not correlated to the advection and can be superimposed afterwards by linearity. Besides, the experimental time scale is much larger than the typical cross-over time between ballistic and diffusive motion (approximately 1 ns) so that we consider the overdamped dynamics. Therefore the governing equation in the streamwise direction is $\partial_t x = \dot{\gamma} z$. Upon integration, one gets:

$$\Delta x \left(\tau\right) = \dot{\gamma} \int_0^\tau \mathrm{d}t\, z \left(t\right). \tag{S23}$$

The mean value of the displacement is thus:

$$\left\langle \Delta x \left(\tau\right) \right\rangle = \dot{\gamma} \int_0^\tau \mathrm{d}t\, \left\langle z \left(t\right) \right\rangle. \tag{S24}$$

In this model, the vertical motion is purely Brownian and is described by the overdamped Langevin equation: $\partial_t z = \sqrt{2D_0}\xi \left(t\right)$, where $\xi \left(t\right)$ is a Gaussian white noise. The corresponding one-dimensional Brownian propagator is:

$$\mathrm{P}_z \left(z, t | z_0, t_0\right) = \frac{1}{\sqrt{2\pi D_0 \left(t - t_0\right)}} \exp \left[-\frac{\left(z - z_0\right)^2}{2 D_0 \left(t - t_0\right)} \right]. \tag{S25}$$

$\mathrm{P}_z \left(z, t | z_0, t_0\right)$ represents the density of probability per unit length for the particle to be located at altitude z at time t, under the condition that the particle was located at z_0 at time t_0. From P_z and Eq. (S24), one obtains $\left\langle \Delta x \right\rangle = \dot{\gamma} \left\langle z_0 \right\rangle \tau$.

Moving to the calculation of the second moment, we have the general form:

$$\langle \Delta x^2 (\tau) \rangle = \dot{\gamma}^2 \int_0^\tau \mathrm{d}t_1 \int_0^\tau \mathrm{d}t_2 \, \langle z(t_1) z(t_2) \rangle, \tag{S26}$$

which can be calculated from the propagator P_z. We note that the averaged quantity $\langle z(t_1) z(t_2) \rangle$ is the product of the particle altitude at time t_1 and the particle altitude at time t_2 for a *unique* trajectory, and consequently:

$$\langle z(t_1) z(t_2) \rangle \neq \int \mathrm{d}z_1 \int \mathrm{d}z_2 \, z_1 \mathrm{P}_z (z_1, t_1 | z_0, t_0) z_2 \mathrm{P}_z (z_2, t_2 | z_0, t_0). \tag{S27}$$

Assuming $t_1 < t_2$, the correct expression is provided by the Markovian properties of Brownian motion and reads:

$$\langle z(t_1) z(t_2) \rangle = \int \mathrm{d}z_1 \int \mathrm{d}z_2 \, z_1 \mathrm{P}_z (z_1, t_1 | z_0, t_0) z_2 \mathrm{P}_z (z_2, t_2 | z_1, t_1). \tag{S28}$$

Knowing that $\int \mathrm{d}z_2 \, z_2 \mathrm{P}_z (z_2, t_2 | z_1, t_1) = z_1$ and choosing $t_0 = 0$, we have:

$$\langle z(t_1) z(t_2) \rangle = \int \mathrm{d}z_1 \, z_1^2 \mathrm{P}_z (z_1, t_1 | z_0, t_0) = z_0^2 + 2D_0 t_1. \tag{S29}$$

Without the assumption $t_1 < t_2$, the latter expression is generalized as:

$$\langle z(t_1) z(t_2) \rangle = z_0^2 + 2D_0 \mathrm{min}(t_1, t_2), \tag{S30}$$

and we note here that $t = t_1 = t_2$ leads to the classical result $\langle z^2(t) \rangle - \langle z(t) \rangle^2 = 2D_0 t$.

In the case of an initial assembly of spatially-distributed identical particles, according to the PDF $\mathcal{P}_0(z_0)$, the latter equation is replaced by its average over z_0:

$$\langle z(t_1) z(t_2) \rangle = \langle z_0^2 \rangle + 2D_0 \mathrm{min}(t_1, t_2). \tag{S31}$$

By inserting this expression in Eq. (S26), one gets:

$$\langle \Delta x^2 (\tau) \rangle = \dot{\gamma}^2 \int_0^\tau \mathrm{d}t_1 \int_0^\tau \mathrm{d}t_2 \, \left[\langle z_0^2 \rangle + 2D_0 \mathrm{min}(t_1, t_2) \right]. \tag{S32}$$

Invoking the decomposition $\int_0^\tau \mathrm{d}t_2 = \int_0^{t_1} \mathrm{d}t_2 + \int_{t_1}^\tau \mathrm{d}t_2$, it follows:

$$\langle \Delta x^2 (\tau) \rangle = \dot{\gamma}^2 \langle z_0^2 \rangle \underbrace{\int_0^\tau \mathrm{d}t_1 \int_0^\tau \mathrm{d}t_2}_{\tau^2} + 2\dot{\gamma}^2 D_0 \int_0^\tau \mathrm{d}t_1 \left(\underbrace{\int_0^{t_1} \mathrm{d}t_2 \, t_2}_{t_1^2/2} + \underbrace{\int_{t_1}^\tau \mathrm{d}t_2 \, t_1}_{(\tau - t_1) t_1} \right), \tag{S33}$$

and thus:

$$\langle \Delta x^2 (\tau) \rangle = \dot{\gamma}^2 \langle z_0^2 \rangle \tau^2 + \frac{2}{3} \dot{\gamma}^2 D_0 \tau^3. \tag{S34}$$

From the above expressions of the average and mean-squared displacements, and adding further the independent contribution due to streamwise Brownian motion, the variance of the streamwise displacement becomes:

$$\sigma_{\Delta x}^2 (\tau) = 2D_0 \tau + \dot{\gamma}^2 \left(\langle z_0^2 \rangle - \langle z_0 \rangle^2 \right) \tau^2 + \frac{2}{3} \dot{\gamma}^2 D_0 \tau^3. \tag{S35}$$

Therefore, the dispersion coefficient can be finally expressed as:

$$\mathcal{D}_x = D_0 + \dot{\gamma}^2 \frac{\langle z_0^2 \rangle - \langle z_0 \rangle^2}{2} \tau + \frac{1}{3} \dot{\gamma}^2 D_0 \tau^2. \tag{S36}$$

The quadratic dependance in lag time τ predicted by the term $\dot{\gamma}^2 D_0 \tau^2/3$ is known and is in agreement with several theoretical [9, 10, 11, 12, 13] and experimental [14, 15, 16] works. The role of the different initial altitudes appears in the additional term $\dot{\gamma}^2 \left(\langle z_0^2 \rangle - \langle z_0 \rangle^2 \right) \tau/2$. This term is linear in lag time and dominates for time scales smaller than the crossover time $\tau_C = 3 \left(\langle z_0^2 \rangle - \langle z_0 \rangle^2 \right)/2D_0$, which corresponds to a typical time needed to diffuse over the standard deviation of the initial distribution $\mathcal{P}_0$ in altitudes z_0.

6.2 Application to uniform distributions of initial altitudes

We focus now on the particular case of uniform distributions of initial particle altitudes. In practice, we specify further the central term $\dot{\gamma}^2 \left(\langle z_0^2 \rangle - \langle z_0 \rangle^2 \right) \tau/2$ obtained in the previous subsection.

The simplest situation, used to obtain the classical formula $\mathcal{D}_x = D_0 \left(1 + \dot{\gamma}^2 \tau^2/3 \right)$, is to consider that all the particles leave from a unique initial altitude z_i. This corresponds to the PDF $\mathcal{P}_0 (z_0) = \delta (z_0 - z_i)$, where δ is the Dirac distribution. From the latter, it follows that $\langle z_0 \rangle^2 = \langle z_0^2 \rangle = z_i^2$, leading to the vanishing of the linear term in lag time in the dispersion coefficient.

A more general situation arises by considering that the particles are initially uniformly distributed over a vertical segment of length nH and centred at altitude z_i, where n is the dimensionless fraction of the typical vertical length H. Note that, when comparing with experimental data (see Fig. 4 in the main article), H denotes the thickness of the observation zone. This situation is described by the PDF:

$$\mathcal{P}_0 (z_0) = \begin{cases} 0 & \text{if } |z_0 - z_i| > nH/2 \\ 1/nH & \text{if } |z_0 - z_i| \leqslant nH/2 \end{cases} . \tag{S37}$$

Thus, the additional term $\dot{\gamma}^2 \left(\langle z_0^2 \rangle - \langle z_0 \rangle^2 \right) \tau/2$ due to the initial distribution of altitudes, can be calculated explicitly by expressing the average initial altitude:

$$\langle z_0 \rangle = \int_0^H \mathrm{d}z_0 \, \mathcal{P}_0 (z_0) \, z_0 = \frac{1}{nH} \int_{z_i - nH/2}^{z_i + nH/2} \mathrm{d}z_0 \, z_0 = z_i, \tag{S38}$$

and the variance in initial altitude:

$$\langle z_0^2 \rangle = \int_0^H \mathrm{d}z_0 \, \mathcal{P}_0 (z_0) \, z_0^2 = \frac{1}{nH} \int_{z_i - nH/2}^{z_i + nH/2} \mathrm{d}z_0 \, z_0^2 = z_i^2 + \frac{(nH)^2}{12}. \tag{S39}$$

Consequently, Eq. (S36) becomes:

$$\mathcal{D}_x (\tau) = D_0 + \dot{\gamma}^2 \frac{(nH)^2}{24} \tau + \frac{1}{3} \dot{\gamma}^2 D_0 \tau^2, \tag{S40}$$

where the weight of the linear term in lag time depends solely on the spatial extent of the initial distribution, but not on the average initial altitude z_i itself. Note that this bulk result is expected to be modified in presence of confinement and interfacial effects. Finally, by invoking the time scale $\tau_z = H^2/D_0$ as in the main article, we obtain the dimensionless equation:

$$\left(\frac{\mathcal{D}_x}{D_0} - 1 \right) (\dot{\gamma} \tau_z)^{-2} = \frac{n^2}{24} \frac{\tau}{\tau_z} + \frac{1}{3} \left(\frac{\tau}{\tau_z} \right)^2 . \tag{S41}$$

We recall that this expression is valid for short lag times τ compared to the Taylor time τ_z/π^2. Interestingly, this single expression allows us to consider various initial uniform distributions, from the classical "dot condition" ($n = 0$) to a complete "line condition" ($n = 1$). As shown in the main article, this equation is in good agreement with our experiments in the short-time limit.

7 Simulation of Langevin equations

In this section, we provide details on the simulations of the Langevin equations, corresponding to the results shown in the main article (see Fig. 4) for comparison with our experimental results and with the analytical models described in the previous sections.

7.1 General Langevin model

For a single Brownian particle of position coordinates x_i, with i the coordinate index, advected in an external flow field characterized by the fluid velocity components v_i, the discrete overdamped Langevin equations read in the Ito convention [17]:

$$x_i\left(t+\delta t\right) = x_i\left(t\right) + v_i\delta t + \frac{D_i\left(t\right)F_i\left(t\right)}{k_{\mathrm{B}}T}\delta t + \partial_{x_i}D_i\mid_{x_i(t)}\delta t + \sqrt{2D_i\left(t\right)\delta t}\,S\left(0,1\right), \quad \text{(S42)}$$

where the diffusion coefficients D_i are non-isotropic and space-dependent in the general case, as a consequence of hydrodynamic interactions with the walls. Here, k_{B} denotes the Boltzmann constant, T the absolute temperature, $S\left(m,\sigma\right)$ a Gaussian distribution with mean value m and standard deviation σ, and F_i the components of the external force exerted on the particle.

More specifically, we consider the bidimensional problem of a Brownian particle advected along x by a linear shear flow near a wall. Gravity is neglected such that the only external force considered is the electrostatic force F_{el} exerted by the wall in the normal direction z. The fluid velocity profile is given by $v_x\left(z\right) = \dot{\gamma}z$, with $\dot{\gamma}$ a constant shear rate. Eq. (S42) thus becomes:

$$x\left(t+\delta t\right) = x\left(t\right) + \dot{\gamma}z\left(t\right)\delta t + \sqrt{2D_x(z\left(t\right))\delta t}\,S\left(0,1\right)\ , \tag{S43}$$

$$z\left(t+\delta t\right) = z\left(t\right) + \partial_z D_z\mid_{z(t)}\delta t + \frac{D_z(z\left(t\right))F_{\mathrm{el}}(z\left(t\right))}{k_{\mathrm{B}}T}\delta t + \sqrt{2D_z(z\left(t\right))\delta t}\,S\left(0,1\right)\ . \tag{S44}$$

For a particle with a radius R, the bulk diffusion coefficient is given by $D_0 = k_{\mathrm{B}}T/6\pi\eta R$, with η the dynamic shear viscosity of the liquid. We introduce the dimensionless variable $Z = z/R$. Due to the hydrodynamic interactions with the wall, the streamwise and wall-normal diffusion coefficients are modified as $D_i = D_0\beta_i$ [18, 2], with:

$$\beta_x\left(Z\right) = 1 - \frac{9}{16}Z^{-1} + \frac{1}{8}Z^{-3} - \frac{45}{256}Z^{-4} - \frac{1}{16}Z^{-5} + O\left(Z^{-6}\right)\ , \tag{S45}$$

$$\beta_z\left(Z\right) = \frac{6(Z-1)^2 + 2(Z-1)}{6(Z-1)^2 + 9(Z-1) + 2}\ . \tag{S46}$$

Finally, the electrostatic force is given by $F_{\mathrm{el}} = -\partial_z\phi_{\mathrm{el}}$, where ϕ_{el} is the repulsive electrostatic potential due to the double layer [1] (see section 2). In the simulations, the van der Waals interactions are neglected.

7.2 Taylor dispersion for tracer particles

We numerically integrate Eqs. (S43) and (S44) with a home-made PYTHON program, see the associated Jupyter notebook (*TaylorDispersion.html*). In order to discuss the main assumption of section 6, we first focus on the simple case of Brownian tracer particles (*i.e.* $\beta_x\left(Z\right) = \beta_z\left(Z\right) = 1$) that are advected in a linear shear flow, within in a closed channel of thickness H, and in the absence of any electrostatic repulsion ($F_{\mathrm{el}} = 0$). We generate 10^4 particle trajectories leaving from initial altitudes described by the uniform distributions defined in the previous section. As such, we consider that the particles are initially located on a line of spatial extent nH. The numerical time step is typically $\delta t = 0.001\tau_z$, and the total duration is approximately $10\tau_z$. Reflective boundary conditions are used at the two walls, *i.e.* at $z = 0$ and $z = H$. The simulations are performed for the dot ($n = 0$), half-line
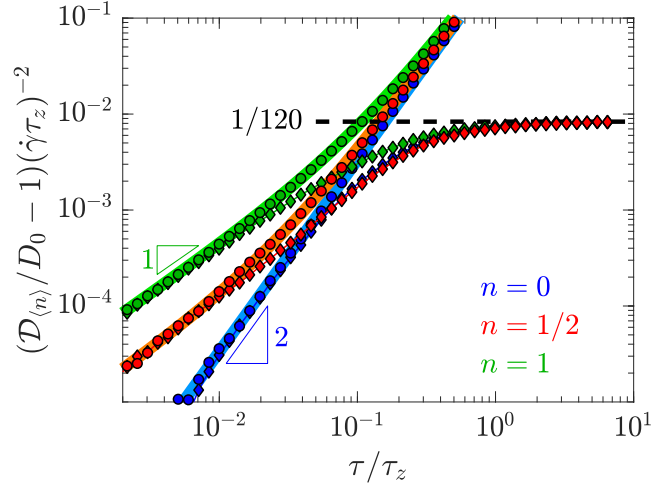
Figure S3: *Reduced dispersion coefficient as a function of dimensionless lag time, from Langevin simulations in free space (circles) and in a confined channel (diamonds), for different initial conditions: dot (blue), half-line (red) and line (green). The coloured plain lines and black dashed line respectively show the theoretical predictions for the short-time (Eq. (S41)) and long-time (Eq. (S19)) limits.*

($n = 1/2$) and line ($n = 1$) conditions. To highlight the relative effect of confinement on the dispersion, we also performed reference simulations in free space (*i.e.* without walls). In all cases, the dispersion coefficient $\mathcal{D}_x$ is calculated from the mean-squared displacement (see section 6) and shown in Fig. S3.

For all conditions, the free-space reduced dispersion coefficient continuously increases with time and is in agreement at all times with the predictions of Eq. (S41). In particular, we clearly observe the expected crossover from the linear to the quadratic behaviours in lag time for particles that are initially broadly distributed in altitudes ($n = 1$).

Furthermore, the Langevin simulation results of the Taylor dispersion in a finite-sized channel are also plotted in Fig. S3. The reduced dispersion coefficients are found to first increase at times shorter than τ_z, following Eq. (S41) as in the free-space case. In contrast to the latter, in the long-time limit, the reduced dispersion coefficient saturates and reaches the constant value predicted by Eq. (S19) no matter the initial particle distribution.

7.3 Effects of hydrodynamic and electrostatic interactions

The previous simulations have been performed without hindered diffusion and electrostatic interactions, which are physical effects that may impact the experiments and that are inherent to nanofluidic settings. We thus performed additional Langevin simulations, including the interactions between the finite-size colloids and the glass wall located at $z = 0$. Simple reflective boundary conditions are maintained at the other boundary, located at $z = H$. The electrostatic parameters were chosen as those that give agreement between the experimental and theoretical SID. Specifically, the particle-wall interaction, ϕ_{el}, is exponentially decaying with magnitude 1.4×10^{-21} J, Debye length 60 nm and thermal energy 4.1×10^{-21} J for input to Eq. S1. Furthermore, at the initial time, the particles are placed in the segments (dot, half-line, line) of the previous section also following the Boltzmann distribution $C(z_c) \propto \exp(-\phi_{el}(z_c)/kT)$. As described by Eqs. (S45) and (S46), we also incorporate non-trivial, hydrodynamic interactions with the wall.

In Fig. S4, we display in red the reduced dispersion coefficients obtained from the Langenvin simulations incorporating electrostatic and hydrodynamic interactions with the wall. These are shown as a function of dimensionless time, using $\tau_z = H^2/D_0$, for all initial conditions. The rescaled dispersion coefficients are found to be systematically smaller than the ones for tracer molecules in finite-sized channels.
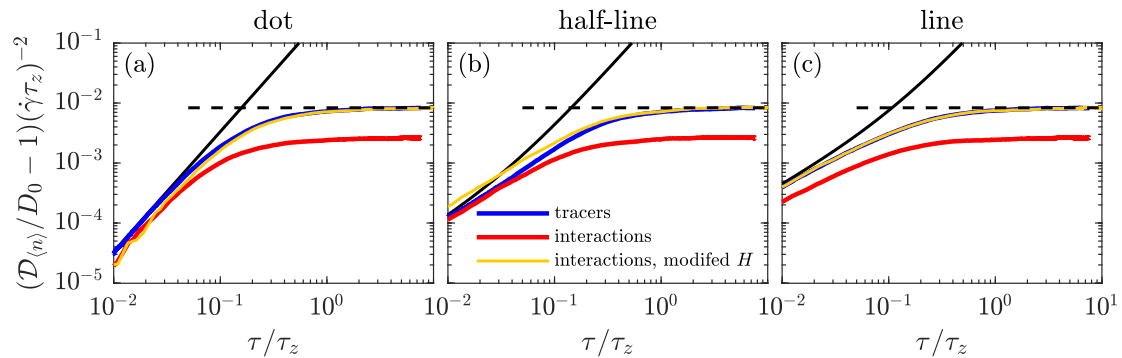
Figure S4: *Reduced dispersion coefficient from (red) Langevin simulations in a channel, including electrostatic repulsion and hindered diffusion induced by the wall located at $z = 0$. These are plotted for three different initial conditions (a,b,c) as a function of dimensionless time. For comparison, we plot the same data (orange) with time on both axes rescaled by the modified time scale $\tau_z = (0.75H)^2/D_0$, and the simulation data of Fig. S3 for (blue) tracer particles in a channel with no interactions with the wall. The lines indicate the asymptotic limits for (horizontal dashed) long times and short times (sloping solid); respectively, a constant value of 1/120 and Eq. 3 in the main paper.*

To justify the difference between tracers and finite-sized, interacting particles, we particularly note that electrostatic forces repel the colloids from the wall, and therefore reduce the area accessible to them. As a secondary effect, the hydrodynamic interactions are thus also reduced since those are maximal at the wall; we will thus assume in the following that D_0 is not modified even while the effect may be slightly operative. As a result of the effectively reduced channel size, the associated timescale should be modified. Therefore, we replot in Fig. S4 the reduced dispersion coefficients versus the dimensionless time by modifying τ_z, using rather $0.75H$, giving a smaller, empirical diffusion time scale $\tau_z = (0.75H)^2/D_0$. We find that the simulation results in the presence of interactions with the wall in an effectively smaller channel of size $0.75\,H$ agree well with the simulation results for tracer particles in the original channel of size H, whatever the initial altitude distributions. This result indicates that the combined effect of electrostatic interactions and hindered diffusion mainly lead – in our experimental range – to a reduced effective time scale τ_z without significantly altering the time dependence itself.

References

[1] Xu Zheng, Fei Shi, and Zhanhua Silber-Li. Study on the statistical intensity distribution (sid) of fluorescent nanoparticles in tirfm measurement. *Microfluidics and Nanofluidics*, 22(11):127, 2018.

[2] Zhenzhen Li, Loïc D'eramo, Choongyeop Lee, Fabrice Monti, Marc Yonger, Patrick Tabeling, Benjamin Chollet, Bruno Bresson, and Yvette Tran. Near-wall nanovelocimetry based on total internal reflection fluorescence with continuous tracking. *Journal of Fluid Mechanics*, 766:147–171, 2015.

[3] B Derjaguin. On the repulsive forces between charged colloid particles and on the theory of slow coagulation and stability of lyophobe sols. *Transactions of the Faraday Society*, 35:203–215, 1940.

[4] Evert Johannes Willem Verwey. Theory of the stability of lyophobic colloids. *The Journal of Physical Chemistry*, 51(3):631–636, 1947.

[5] Dennis C Prieve. Measurement of colloidal forces with tirm. *Advances in Colloid and Interface Science*, 82(1-3):93–125, 1999.

[6] AJ Goldman, RG Cox, and H Brenner. Slow viscous motion of a sphere parallel to a plane wall—ii couette flow. *Chemical Engineering Science*, 22(4):653–660, 1967.

[7] Albert Einstein. Über die von der molekularkinetischen theorie der wärme geforderte bewegung von in ruhenden flüssigkeiten suspendierten teilchen. *Annalen der physik*, 322(8):549–560, 1905.

[8] Geoffrey Ingram Taylor. Dispersion of soluble matter in solvent flowing slowly through a tube. *Proceedings of the Royal Society of London. Series A. Mathematical and Physical Sciences*, 219(1137):186–203, 1953.

[9] TGM Van de Ven. Diffusion of brownian particles in shear flow. *Journal of Colloid and Interface Science*, 62(2):352–355, 1977.

[10] GK Batchelor. Mass transfer from a particle suspended in fluid with a steady linear ambient velocity distribution. *Journal of Fluid Mechanics*, 95(2):369–400, 1979.

[11] RT Foister and TGM Van De Ven. Diffusion of brownian particles in shear flows. *Journal of Fluid Mechanics*, 96(1):105–132, 1980.

[12] C Van den Broeck, JM Sancho, and M San Miguel. Harmonically bound brownian motion in flowing fluids. *Physica A: Statistical Mechanics and its Applications*, 116(3):448–461, 1982.

[13] Kunimasa Miyazaki and Dick Bedeaux. Brownian motion in a fluid in simple shear flow. *Physica A: Statistical Mechanics and its Applications*, 217(1-2):53–74, 1995.

[14] Hiroshi Orihara and Yoshinori Takikawa. Brownian motion in shear flow: Direct observation of anomalous diffusion. *Physical Review E*, 84(6):061120, 2011.

[15] Einar Orn Fridjonsson, Joseph D Seymour, and Sarah L Codd. Anomalous preasymptotic colloid transport by hydrodynamic dispersion in microfluidic capillary flow. *Physical Review E*, 90(1):010301, 2014.

[16] Yoshinori Takikawa, Takahiro Nunokawa, Yuji Sasaki, Makoto Iwata, and Hiroshi Orihara. Three-dimensional observation of brownian particles under steady shear flow by stereo microscopy. *Physical Review E*, 100(2):022102, 2019.

[17] Donald L Ermak and J Andrew McCammon. Brownian dynamics with hydrodynamic interactions. *The Journal of chemical physics*, 69(4):1352–1360, 1978.

[18] Luc P Faucheux and Albert J Libchaber. Confined brownian motion. *Physical Review E*, 49(6):5158, 1994.